Recombination and bandgap engineering in CdSeTe/CdTe solar cells

Cite as: APL Mater. 7, 071112 (2019); doi: 10.1063/1.5098459
Submitted: 2 April 2019 • Accepted: 13 June 2019 •
Published Online: 22 July 2019

View Online Export Citation CrossMark

X. Zheng,[1,2] D. Kuciauskas,[1] J. Moseley,[1] E. Colegrove,[1] D. S. Albin,[1] H. Moutinho,[1] J. N. Duenow,[1] T. Ablekim,[1] S. P. Harvey,[1] A. Ferguson,[1] and W. K. Metzger[1]

AFFILIATIONS

[1] National Renewable Energy Laboratory, 15013 Denver West Pkwy., Golden, Colorado 80401, USA
[2] University of Illinois at Chicago, 1200 W. Harrion St., Chicago, Illinois 60607, USA

ABSTRACT

Selenium compositional grading in CdTe-based thin-film solar cells substantively improves carrier lifetime and performance. However, where and how recombination lifetime improves has not been studied significantly. Here, we deposit a $CdSe_xTe_{1-x}$/CdTe bilayer on $MgZnO/SnO_2$/glass, which achieves a short-circuit current density greater than 28 mA/cm^2 and carrier lifetimes as long as 10–20 ns. We analyze the grain structure, composition, and recombination through the thickness of the absorber using electron backscatter diffraction, Auger-electron spectroscopy, cathodoluminescence spectrum imaging, and time-resolved photoluminescence microscopy. Despite small CdSeTe grains near the pn-junction and significantly larger CdTe grains in the rest of the film, both time-resolved photoluminescence and cathodoluminescence reveal that the carrier lifetime in CdSeTe alloy regions is longer than in CdTe regions. The results indicate that Se both passivates grain boundaries and improves grain-interior carrier lifetime. However, these effects occur only where there is significant alloying, which is important for bandgap engineering.

I. INTRODUCTION

Thin-film polycrystalline CdTe-based solar cells have reached 22.1% cell efficiency.[1] More importantly, commercial modules have reached efficiencies of 17%–18% at costs competitive with conventional energy sources, and they have superior temperature coefficient and spectral response relative to silicon and other solar technologies.[2,3] Eliminating the CdS window layer and introducing $CdSe_xTe_{1-x}$ (CdSeTe) bandgap grading contributed to the steady increase in small-area research cell efficiency from 16% to 22.1%. CdSeTe has helped increase photocurrent by lowering the energy bandgap but without commensurate open-circuit voltage (V_{oc}) losses. This is attributed in part to longer carrier lifetimes relative to CdTe-only absorbers.[4] The regions and physical mechanisms where CdSeTe produces longer carrier lifetime in CdSeTe/CdTe devices are critical to bandgap engineering.

To examine these issues, we have fabricated a CdSeTe/CdTe device structure represented by the schematic in Fig. 1(a) and compared this to the same device structure without Se in the absorber (labeled CdTe device). Figure 1(b) illustrates from modeling[5] that while the bandgap is about 80 meV lower for the CdSeTe/CdTe bilayer cell near the interface, for small interfacial offsets and hole density in the low 10^{14} cm^{-3}, the overall band bending is not expected to differ substantively in the two devices. After the $CdCl_2$ treatment, Se diffuses into the CdTe region both along the grain boundaries (GBs) and in the grain interior (GI). It is not clear how much the lifetime throughout will be adjusted by varying Se levels, ranging from an alloy at the front to impurity levels (<1%) in the back of the cell. Here, we apply one-photon (1PE) and two-photon excitation (2PE) time-resolved spectroscopy using time-correlated single-photon counting[6] to profile recombination throughout CdSeTe/CdTe solar cells and contrast this with a CdTe solar cell. We also characterize the structural and chemical changes throughout the CdSeTe/CdTe device by Auger-electron spectroscopy (AES) profiling, electron backscatter diffraction (EBSD) on device cross sections, and room-temperature cathodoluminescence (CL) spectrum imaging on beveled devices.

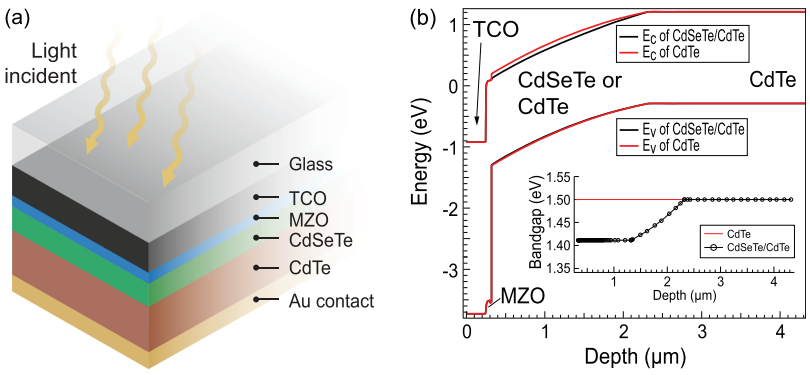

FIG. 1. (a) A schematic (not to scale) of the CdSeTe/CdTe device and (b) modeled band alignment for CdTe (red) and CdSeTe/CdTe (black) solar cells.

II. EXPERIMENT

Polycrystalline CdSeTe thin films were deposited on MgZnO(MZO)/TEC glass substrates by close-spaced sublimation (CSS).[7,8] A CdSe layer was not deposited at any stage of device fabrication.[9] Instead, films were deposited using a CdSeTe alloy source by CSS, which can be challenging. Because elemental vapor pressures vary at 600 °C–700 °C, here we limit the total pressure to below 0.12 Torr without intentional oxygen in the CSS chamber and use fine CdSeTe alloy powder sources and a large temperature difference between the source and the substrate.[10,11] Before deposition, samples are preheated for 10 min at 600 °C with the source temperature at 500 °C to stabilize vapor flux from the source. This is followed by an 80-s deposition with the substrate temperature at 480 °C and the source temperature at 670 °C. After CdSeTe is deposited, a CdTe layer is deposited in the same chamber with the substrate temperature at 625 °C and the source temperature at 660 °C with 20 Torr He in the ambient. Due to changes in the lattice energy as a function of composition, CdSeTe can have a higher activation energy for recrystallization and grain growth than binary CdTe.[11] Here, after deposition, the CdSeTe/CdTe film is treated with $CdCl_2$ at 460 °C for 10 min with 400-Torr He ambient.[12] The back contact is formed using a wet $CuCl_2$ treatment followed by evaporation of a 100-nm Au back contact.[13]

III. RESULTS

Devices without Se incorporation had a power conversion efficiency of 12.5% with a relatively high V_{oc} of 871 mV, as shown by the current density-voltage (JV) plot in Fig. 2(a). By introducing Se into the absorber, short-circuit current density (J_{sc}) increases from 25.2 mA/cm^2 to 28.5 mA/cm^2, which compensates for the V_{oc} loss from 871 mV to 815 mV, and efficiency increases to >15%. The external quantum efficiency (EQE) in Fig. 2(b) indicates how CdSeTe increases photocurrent by collecting more light in the red spectral region. Integrating the EQE spectra from 300 nm to 900 nm gives an estimated J_{sc} of 25.7 mA/cm^2 for CdTe and 28.6 mA/cm^2 for CdSeTe/CdTe, which are in good agreement with the JV data. To determine average carrier lifetimes, time-resolved photoluminescence (TRPL) with a 640-nm excitation wavelength was measured through the glass at a laser repetition rate of 1.1 MHz with unfocused excitation (0.3-mm excitation spot diameter and 1-mW average power) and emission detection between 800 and 920 nm. Fast (τ_1) and slow (τ_2) decay components are independent of the detection wavelength and were determined from a biexponential fit to the data over the region of 50%–0.5% of the maximum counts. Simulations indicate that at such excitation conditions, the space-charge field is largely screened by the photogenerated carriers and the slower TRPL decay component is similar to the bulk carrier lifetime.[14–16] TRPL analysis indicates that Se incorporation increased τ_1 from 0.8 ns to 1.7 ns and τ_2 from 3.2 ns to 14 ns in the CdTe and CdSeTe/CdTe devices, respectively.

The correlations of the Se content to grain size and orientation were measured throughout the CdSeTe/CdTe absorber by Auger depth profiling and cross-sectional EBSD. The EBSD cross-sectional inverse-pole-figure (IPF) map in Fig. 3(a) clearly reveals a bilayer structure with smaller grains in the CdSeTe region at the

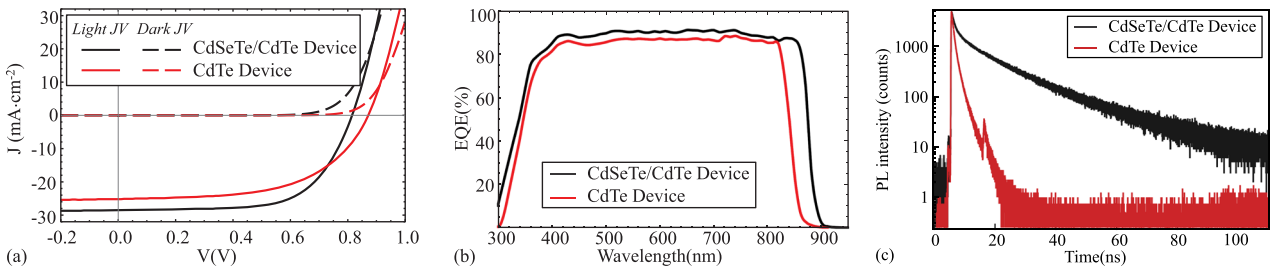

FIG. 2. Comparison of (a) JV, (b) EQE, and (c) TRPL results for CdTe and graded CdSeTe/CdTe solar cells.

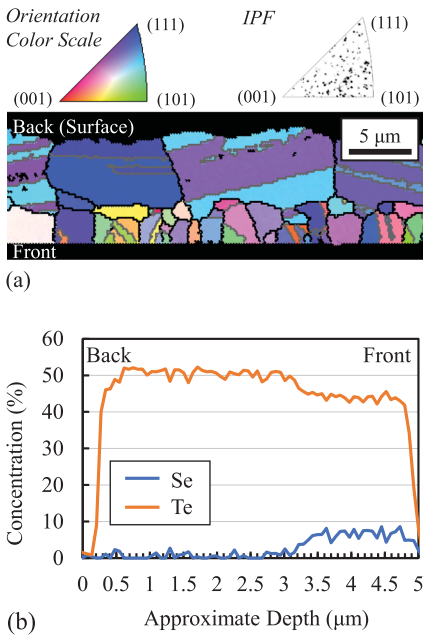

FIG. 3. (a) Cross-sectional IPF EBSD map and inverse pole figure showing orientations normal to the sample surface. (b) Auger profile of Se and Te distribution through the whole device.

front of the device and very large grains in the back of the film in the CdTe region. The pole figure histogram for the full map does not indicate grain orientation texture after the $CdCl_2$ treatment. The AES profile in Fig. 3(b) shows that the Se concentration falls from about 8% at the front interface to noise levels about 2 μm from the interface. The Se gradient after the first 1.5 μm shows Se interdiffusion into CdTe after CSS CdTe deposition and $CdCl_2$ annealing.

Figures 4(a)–4(e) summarize room-temperature CL spectrum imaging data collected on surfaces formed by focused-ion-beam milling to make bevels through the device layers at a 20° angle with respect to the horizontal.[17] In CL spectrum imaging, which is distinct from conventional CL imaging, a full luminescence spectrum is recorded at each image pixel. Figure 4(a) is an image of the integrated intensity from 1.27 eV to 1.73 eV, which is scaled according to the maximum and minimum pixel intensities. The back two-thirds of the device are faintly visible in this image but can be seen clearly by adjusting the contrast and brightness as shown in Fig. 4(b). Figure 4(c) is a map of the peak photon energies extracted from the CL spectra, which are roughly equal to the room-temperature bandgap energies. In addition, Fig. 4(c) illustrates that Se diffuses into CdTe along some of the GBs (see the white arrow). However, this GB diffusion fails to passivate and make the GBs visibly brighter in the CL image. Figure 4(d) plots the horizontally averaged intensity and peak photon energy as a function of distance from the front interface. This plot shows that the maximum CL intensity occurs within CdSeTe and is about 3–4 times greater than the CdTe CL

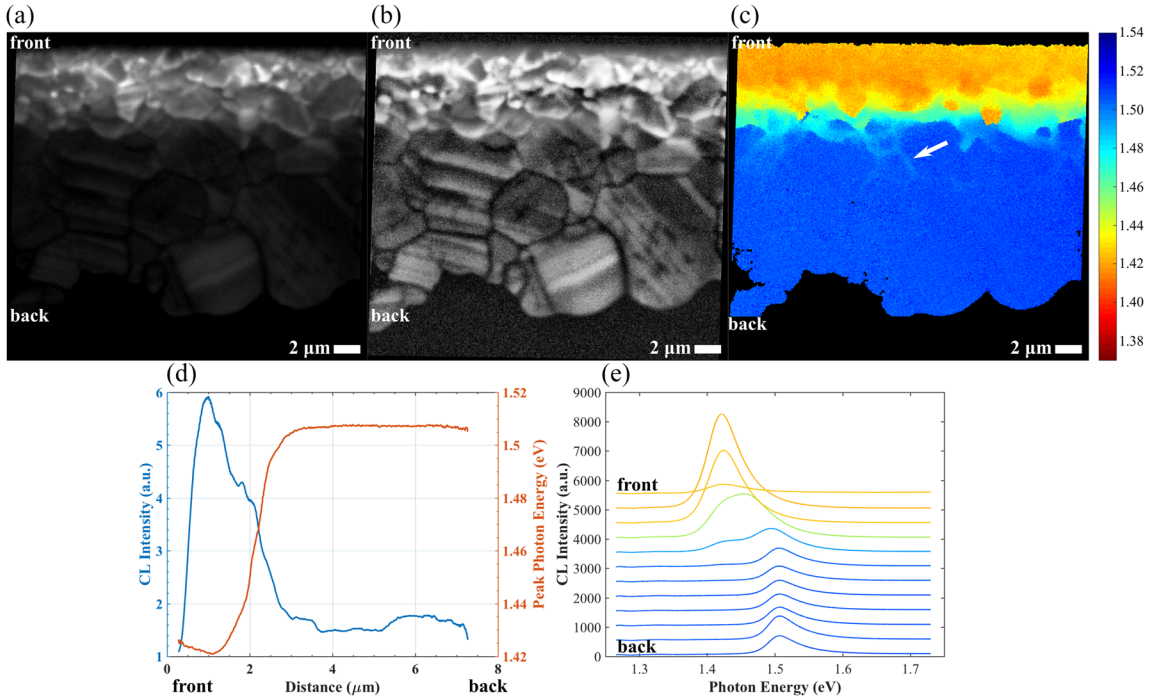

FIG. 4. Room-temperature CL data on a beveled CdSeTe/CdTe device: (a) integrated-intensity image, (b) intensity image with contrast and brightness adjusted to show the relatively dark CdTe grains, (c) peak-photon energy map, (d) horizontally averaged intensity and peak photon energy plotted as function of distance from the front interface, and (e) horizontally averaged spectra from the front to the back of the device in which each spectrum is colored according to its peak energy on the color scale given in (c).

intensity—despite smaller grains in the CdSeTe region at the front of the device. The evolution in the peak photon energy from the front to the back can be seen in the horizontally averaged CL spectra in Fig. 4(e). Figures 4(a)–4(e) indicate that the CdSeTe alloyed region in roughly the front third of the device has a much greater intensity than CdTe in the rest of the film; the intensity correlates inversely with the peak photon energy and bandgap and directly with the Se concentration. The minimum CdSeTe bandgap is found to be 1.42 eV, consistent with the AES data [Fig. 3(c)], and the CdTe bandgap is 1.5 eV, as expected.

The CL does not give a direct measure of carrier lifetime. To evaluate bulk carrier lifetime and GB recombination in a Se graded absorber, we used 2PE TRPL microscopy with laser excitation at a wavelength of 1030 nm. This analysis was earlier developed for device back-side measurements.[18] In this study, a long-working-distance microscope objective enabled 2PE TRPL microscopy measurements through 3-mm glass. In this way, carrier lifetimes were compared near the MZO/CdSeTe interface [emission at 1.42 eV, Fig. 5(c)] and in CdTe [emission at 1.50 eV, Fig. 5(d)]. Integrated TRPL microscopy data taken at different locations across the sample are essentially identical, indicating that the TRPL microscopy data in Fig. 5 are representative of the device.

Figures 5(a) and 5(b) illustrate the spatial variation of PL emission intensity in the CdTe (excitation through back) and the CdSeTe (excitation through glass) regions, respectively. The tight focus can introduce diffusion and injection effects distinct from the large 1PE spot size measurements presented in Fig. 2.[19] The spatial resolution is lower when measured through the glass; nonetheless, regions with stronger and weaker PL emission can still be

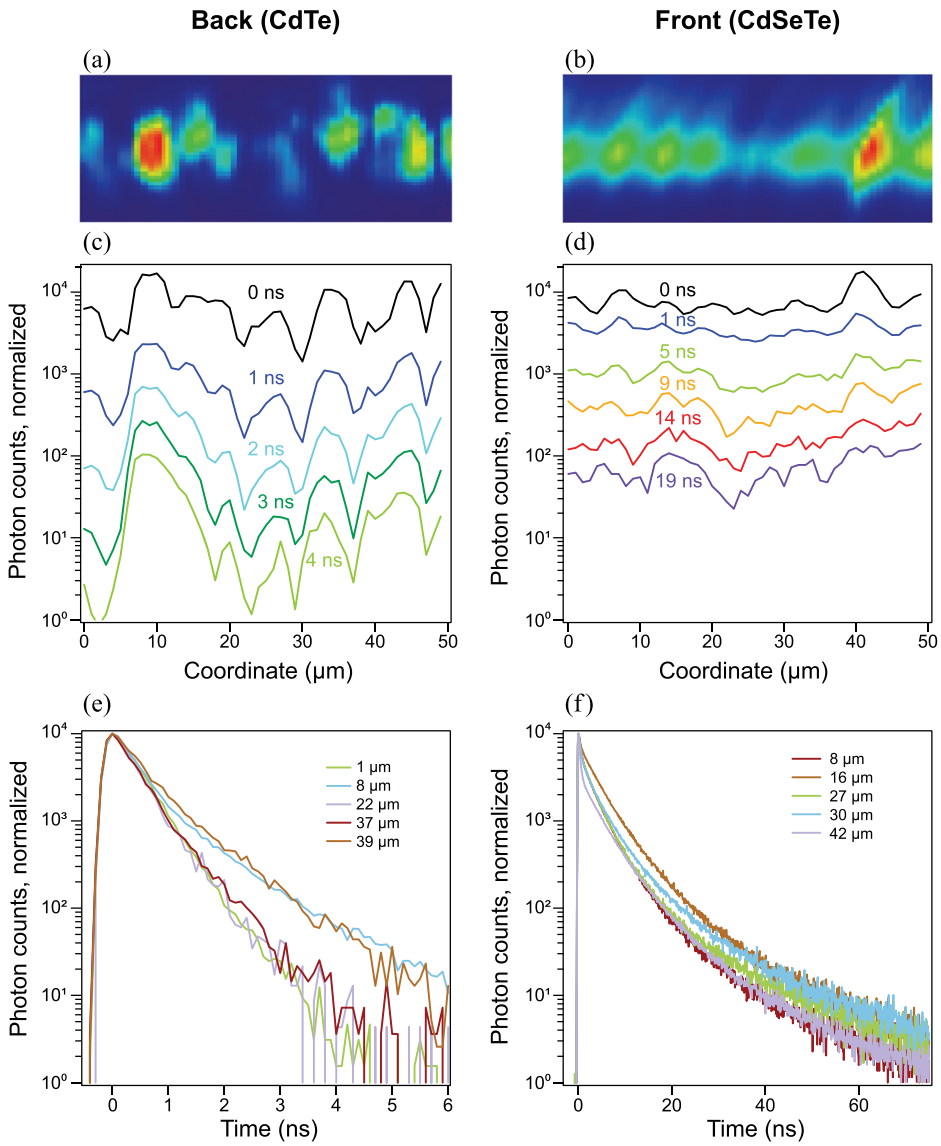

FIG. 5. [(a) and (b)] Integrated PL intensity, [(c) and (d)] linear PL intensity profiles at different times after the excitation (like colors correspond to similar times), and [(e) and (f)] TRPL decays at different locations for CdTe (back, left column) and CdSeTe (front, right column) regions of the same bilayer solar cell.

resolved in both cases. Figures 5(a) and 5(b) illustrate that PL photon counts across the back CdTe surface have far more variation than the front CdSeTe region, and it is plausible that the former are caused by GBs. In Fig. 5(c), the lateral intensity varies by about 1 order of magnitude initially, and by 2 orders of magnitude after 4 ns. For CdSeTe, shown in Fig. 5(d), the contrast in TRPL data remains about the same, varying only by a factor of 2–3, even when the time scale is longer [19 ns in Fig. 5(d) vs 4 ns in Fig. 5(c)]. This would imply that the impact of GB recombination is much larger for the CdTe region of the graded device. This is consistent with the CL intensity data shown in Figs. 4(a) and 4(b), where the CdTe region has clear and dark GB contrast relative to the CdSeTe region.

We plotted several corresponding TRPL decays in the CdTe region [Fig. 5(e)] and the CdSeTe region [Fig. 5(f)] at different positions across the device. In the CdTe region, the TRPL decay can be described as single exponential with $\tau \approx 0.45$ ns, which would correspond to a GB recombination velocity of $S_{GB} \approx 10^5$ cm/s. This recombination velocity is typical for CdTe,[20,21] and these data are consistent with the CL data in Fig. 4, where GBs are dark near the back contact of the device.

By contrast, in the CdSeTe region shown in Fig. 5(f), TRPL curves taken from different locations all decay about an order-of-magnitude more slowly, corresponding to an upper limit of $S_{GB,CdSeTe} < 10^4$ cm/s. Enhanced S_{GB} sensitivity measurements will require further development and studies. The TRPL microscopy data are consistent with the CL data shown in Figs. 4(a) and 4(b). The lifetimes are significantly longer in CdSeTe, and GB recombination appears to be reduced by an order of magnitude. These observations help describe how the relatively small CdSeTe grains at the front of the device exhibit longer lifetimes than CdTe regions with larger grains.

IV. CONCLUSION

CdSeTe/CdTe devices were fabricated, compared with CdTe-only devices, and characterized throughout the device depth. In CdSeTe/CdTe devices, Se alloying effectively lowers the bandgap, thereby increasing photocurrent without commensurate V_{oc} losses, resulting in increased efficiency relative to CdTe-only devices. Auger profiles on CdSeTe/CdTe devices indicate about 8% Se incorporation at the front interface that corresponds with a layer of small CdSeTe grains as revealed by EBSD. CL spectra corroborate the AES compositional changes and show about a factor of four enhanced CL intensity in CdSeTe regions relative to CdTe—despite significantly smaller CdSeTe grains. CdTe GBs are very dark relative to their GI or CdSeTe regions. The CL data are consistent with 1PE TRPL measurements, where CdTe-only devices have inferior lifetime compared to CdSeTe/CdTe devices. Within the CdSeTe/CdTe devices, 2PE microscopy again confirms that CdSeTe has a longer lifetime and corroborates significant CdSeTe GB passivation. Se diffusion along the GBs during the $CdCl_2$ treatment or in the GI at levels below AES sensitivity fails to show improved lifetime or enhanced CL intensity. Instead, alloying levels of Se appear necessary to significantly reduce GI and GB recombination. Consequently, trade-offs in lifetime and bandgap throughout the absorber layer must be taken into account when bandgap engineering CdSeTe/CdTe solar technology.

ACKNOWLEDGMENTS

This work was authored by the National Renewable Energy Laboratory, operated by the Alliance for Sustainable Energy, LLC, for the U.S. Department of Energy (DOE) under Contract No. DE-AC36-08GO28308. This material is based in part upon work supported by the U.S. Department of Energy's Office of Energy Efficiency and Renewable Energy (EERE) under Solar Energy Technologies Office (SETO) Agreement No. 34353. The views expressed in the article do not necessarily represent the views of the DOE or the U.S. government. The U.S. government retains and the publisher, by accepting the article for publication, acknowledges that the U.S. government retains a nonexclusive, paid-up, irrevocable, worldwide license to publish or reproduce the published form of this work, or allow others to do so, for U.S. government purposes.

REFERENCES

[1] M. A. Green, Y. Hishikawa, E. D. Dunlop, D. H. Levi, J. Hohl-Ebinger, and A. W. H. Ho Baillie, Prog. Photovoltaics **26**, 3–12 (2017).
[2] See https://www.lazard.com/media/450337/lazard-levelized-cost-of-energy-version-110.pdf for Lazard's Levelized Cost of Energy Analysis-Version 11.0; accessed February 15, 2019.
[3] See http://www.firstsolar.com/-/media/First-Solar/Technical Documents/Series-6-Datasheets/Series-6-Datasheet.ashx for information on module efficiency and temperature coefficients; accessed February 15, 2019.
[4] M. Gloeckler, I. Sankin, and Z. Zhao, IEEE J. Photovoltaics **3**, 1389–1393 (2013).
[5] T. Ablekim *et al.*, ACS Appl. Energy Mater. **1**, 5135–5139 (2018).
[6] D. V. O'Connor and D. Phillips, *Time-Correlated Single Photon Counting* (Academic Press, San Diego, CA, 1984).
[7] D. H. Rose *et al.*, Prog. Photovoltaics **7**, 331 (1999).
[8] T. Ablekim *et al.*, IEEE J. Photovoltaics **9**, 888–892 (2019).
[9] J. D. Poplawsky, W. Guo, N. Paudel, A. Ng, K. More, D. Leonard, and Y. Yan, Nat. Commun. **7**, 12537 (2016).
[10] K. C. Mills, *Thermodynamic Data for Inorganic Sulphides* (Selenides and Tellurides, 1987), pp. 729–733; A. G. Sigai and H. Wiedemeier, J. Electrochem. Soc. **119**, 910–914 (1972).
[11] B. MacDonald, A. Martucci, S. Rubanov, S. Watkins, P. Mulvaney, and J. Jasieniak, ACS Nano **6**, 5995 (2012).
[12] M. Amarasinghe *et al.*, Adv. Energy Mater. **8**, 1702666 (2018).
[13] D. Mao, D. Blatz, C. E. Wickersham, Jr., and M. Gloeckler, Sol. Energy Mater. Sol. Cells **157**, 65 (2016).
[14] W. K. Metzger, R. K. Ahrenkiel, J. Dashdorj, and D. J. Friedman, Phys. Rev. B **71**, 035301 (2005).
[15] W. K. Metzger, M. J. Romero, P. Dippo, and M. Young, in *Conference Record of the 2006 IEEE 4th World Conference on Photovoltaic Energy Conversion* (IEEE, 2006), Vol. 1, p. 372.
[16] A. Kanevce, D. H. Levi, and D. Kuciauskas, Prog. Photovoltaics: Res. Appl. **22**, 1138–1146 (2014).
[17] F15EI xT-Nova Nanolab, Moseley, JAP, 2017.
[18] D. Kuciauskas, D. Lu, S. Grover, G. Xiong, and M. Gloeckler, Appl. Phys. Lett. **111**, 233902 (2017).
[19] D. Kuciauskas, T. H. Myers, T. M. Barnes, S. A. Jensen, and A. M. Allende Motz, Appl. Phys. Lett. **110**, 083905 (2017).
[20] J. Moseley *et al.*, J. Appl. Phys. **124**, 113104 (2018).
[21] A. Kanevce, J. Moseley, M. Al-Jassim, and W. K. Metzger, IEEE J. Photovoltaics **5**, 1722 (2015).